Compact Plasmonic Blackbody for Cancer Theranosis in Near-Infrared II Window

Jiajing Zhou,[†,‡] *Yuyan Jiang,*[†,‡] *Shuai Hou,*[†] *Paul Kumar Upputuri,*[†] *Di Wu,*[†, §] *Jingchao Li,*[†] *Peng Wang,*[†] *Xu Zhen,*[†] *Manojit Pramanik,*[†] *Kanyi Pu**[,†] *and Hongwei Duan**[,†]

[†]School of Chemical and Biomedical Engineering, Nanyang Technological University, 70 Nanyang Drive, Singapore 637457

[§] Department of Chemistry, Zhejiang University, Hangzhou 310028, China

KEYWORDS: plasmonic blackbody, hyperbranched nanostructure, photothermal conversion, polydopamine, second near-infrared window

ABSTRACT

We have developed a class of blackbody materials, *i.e.*, hyperbranched Au plasmonic blackbody (AuPB) of compact sizes (< 50 nm). The AuPB was prepared in a seedless and surfactant-free approach based on the use of mussel-inspired dopamine. Strong intraparticle plasmonic coupling among branches in close proximity leads to intense and uniform broadband absorption across 400-1350 nm. The blackbody absorption imparts the compact AuPB with a superior photothermal efficiency of >80% and closely matched photothermal activity in the first near-infrared (NIR-I) and the second near-infrared (NIR-II) spectral windows, making it a rare broadband theranostic probe for integrated photoacoustic imaging and photothermal therapy (PTT). Our comparative study, using the same probe, has demonstrated that the improved PTT outcome of NIR-II than NIR-I primarily results mainly from its higher maximum permission exposure (MPE) rather than the deeper tissue penetration favored by longer wavelengths. The compact plasmonic broadband nano-absorbers with tailored surface properties hold potentials for a wide spectrum of light-mediated applications.

Highly efficient photothermal conversion covering a wide spectral window is in great demands for diverse applications ranging from solar energy conversion and photocatalysis to optical devices and nanomedicine.[1-5] A blackbody is an ideal broadband photoabsorber because it theoretically absorbs all lights of different wavelength and polarization that shine on it.[6] In fact, a real blackbody is not yet available since photoabsorbers naturally have preferential absorption wavelengths dependent on their composition and structural details. Only very few examples were reported showing nearly perfect blackbody absorption in certain spectral ranges.[7-9] Localized surface plasmon resonance (LSPR) of plasmonic metal nanostructures can be flexibly tailored by modulating their chemical compositions, structural parameters, and local environment.[10-13] Excited LSPR dissipates energy of incident light by the combination of Mie scattering and absorption-mediated thermal conversion, making plasmonic nanostructures compelling photoabsorbers.[14-16] Notably, broadband LSPR are generally induced by strong plasmonic coupling between closely arranged building blocks.[17-19] However, forming ensembles consisting of multiple components tend to reduce absorption efficiency due to strong light scattering resulting from their large sizes.[20,21] Thereby, it remains challenging to produce a compact plasmonic blackbody with efficient broadband photo-absorption.

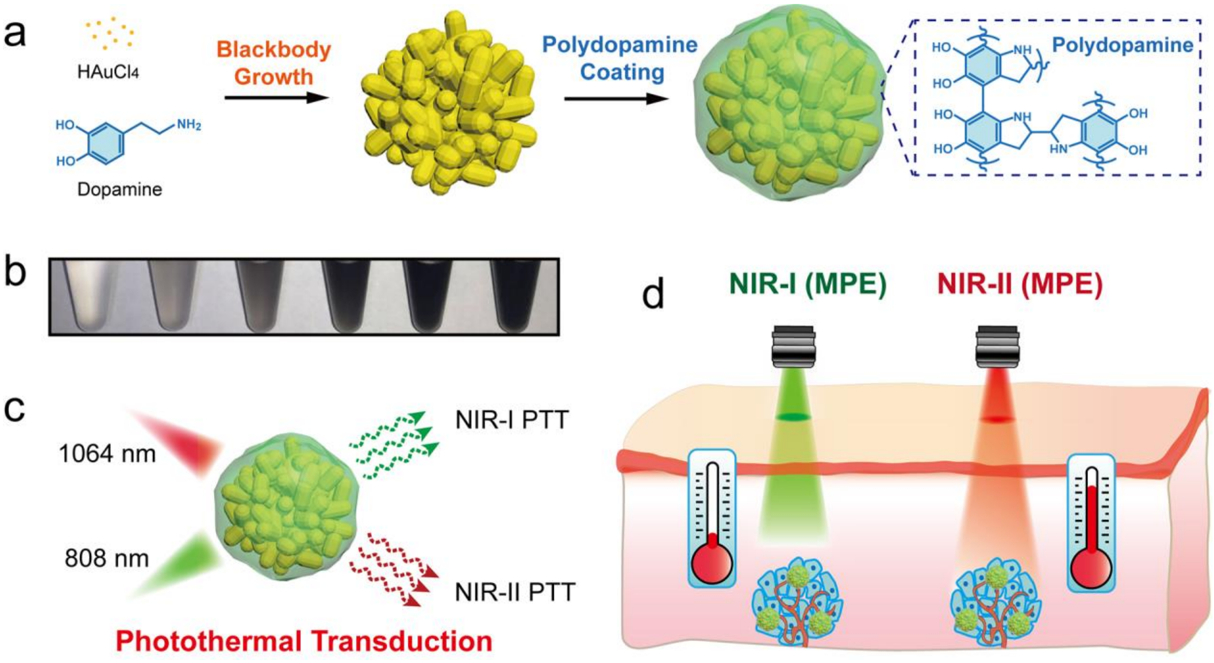

Figure 1. (a) Schematic illustration of the one-pot synthesis of AuPBs. (b) Photographs of aqueous dispersion of AuPBs at varying concentrations (0, 25, 50, 100, 200, and 500 μg/mL). (c) Schematic of AuPBs with closely matched photothermal activity across the NIR spectral range. (d) Comparative photothermal cancer therapy of AuPBs under maximum permission exposure (MPE) of NIR-I and NIR-II irradiation.

Here, we report a one-pot seedless and surfactant-free approach based on the use of mussel-inspired dopamine to synthesizing compact, monodispersed Au plasmonic blackbody (AuPB) with a hyperbranched internal structure. A key finding is that the high density of randomly oriented branches supports enormous intraparticle coupling, which affords uniform broadband absorption spanning the entire UV-Vis-NIR range (400-1350 nm) in plasmonic nanostructures of compact sizes (< 50 nm). As illustrated in Figure 1a, dopamine not only serves as both reducing agents and surface capping ligands, spontaneous self-polymerization of dopamine also leads to highly adhesive polydopamine coating on the AuPBs, imparting them with robust, readily tailorable surface chemistry and excellent thermal stability. We have shown that the AuPBs at a concentration as low as 0.02% (w:w) is sufficient to achieve complete darkness (Figure 1b).

Light-activated phototherapy and bioimaging modalities such as photothermal therapy (PTT) and photoacoustic imaging (PAI) hold great potential for clinical translation.[22-25] The use of PTT was primarily focused on superficial lesions because of limited penetration depth of ultraviolet and visible (UV-Vis) light sources.[22,26] The discovery of biologically transparent near-infrared (NIR) spectral window (650-1350 nm) provides opportunities for PTT in deep tissue applications.[27,28] Likewise, PAI that detects ultrasound signal generated from light-mediated thermal expansion is also expected to benefit from improved signal-to-background ratio and tissue penetration.[29] In particular, there is growing interest in the second NIR (NIR-II) window (1000-1350 nm) that offers further improved light penetration, lower background signal, and higher maximum permission exposure (MPE), compared to the traditional first NIR (NIR-I) window (650-950 nm).[30-34] Great efforts are made to develop efficient phototherapy transduction agents and imaging probes. However, no definitive evidence is yet available for developing a guideline to optimized NIR-II light-mediated diagnosis and therapy, largely due to the lack of photoabsorbers with closely matched activity across a broad spectral range (Figure 1c). In this study, we have demonstrated that the compact AuPBs make it possible to address this open question in a mouse tumor model. Importantly, our *in vitro* and *in vivo* results have confirmed that the most significant benefit of NIR-II PTT lies in the higher MPE of the NIR-II light rather than the better tissue penetration (Figure 1d). The theranostic AuPBs with excellent NIR-II activity offers the opportunities for safe, efficient detection and treatment of deep tissue lesions.

RESULTS AND DISCUSSION

We have found that reduction of $HAuCl_4$ (0.1 mg/mL) by dopamine (0.2 mg/mL) in tris(hydroxymethyl)aminomethane (TRIS) buffer produced highly uniform AuPBs of around 45 nm (Figure 2a,b and S1). Transmission electron microscopy (TEM) observation reveals that the AuPBs feature a hyperbranched framework of nanorods of 5 nm in width. LSPR of plasmonic nanostructures is highly sensitive to their morphology and the changes of local environment in close proximity, and is an excellent indicator for monitoring the structural evolution. UV-Vis-NIR spectra (Figure 2c) show that broadband absorption already appeared after 30 min of reaction, and the relative ratio of absorption at 1064 and 808 nm increased from 0.52 at 30 min to the maximum of 0.94 at 6 h (Figure S2). In contrast to the clear solution of dopamine, the as-prepared AuPB dispersion is completely black (inset in Figure 2c). Surface ligands play key roles in the anisotropic growth of nanocrystals.[35,36] Dopamine goes through oxidation into dopaminequinone, intramolecular cyclization, and oxidative oligomerization/self-assembly to self-polymerize into polydopamine under weak basic conditions.[37,38] Pyrocatechol that does not have this property was used as a control for a better understanding of the role of dopamine. Our experiments show that introducing $HAuCl_4$ precursor into pyrocatechol solution led to rapid color change to pink red and further to purple within 5 min (Figure S3). In contrast, the reaction mixture in dopamine solution initially was light-yellow and became darker gradually over the course of 8 h. This difference suggests that $HAuCl_4$ was rapidly reduced into Au nanoparticles by pyrocatechol, whereas Au^+ complex was formed in the dopamine system,[39] which slowly grew into the hyperbranched nanostructure. Consistent with this analysis is that the use of pyrocatechol only resulted in irregular solid Au nanoparticles (Figure S3). On the other hand, TEM images of the nanoparticle retrieved during the growth in dopamine solution show that multipod nanocrystals around 15 nm formed in the first hour, with short branches (5 nm in diameter and 7 nm in length) emanating from a core (Figure 2d). Subsequently, the branches continued to grow and diverge in a geometric progression by continual deposition of Au, and eventually transformed into a disordered hyperbranched superstructure (Figure 2e-g). Self-polymerized polydopamine is known to strongly bond to virtually any solid substrates.[37,40,41] We reason that the strong binding of polydopamine induces anisotropic deposition of Au atoms, leading to consistent divergence of branches during the slow growth, as shown in the structural evolution observed in TEM images (Figure 2d-g). Polydopamine coating (Figure 2b) potentially serves as a shield to isolate individual nanorods and prevent overgrowth of the nanorods into a solid structure, affording the hyperbranched structures with abundant built-in electromagnetic hotspots. The size of the nanocrystals is determined by the feeding ratio of $HAuCl_4$ and dopamine. When the ratio was gradually changed from 0.5 to 2.0, the size of nanoparticles increased from 45 to 250 nm (Figure S4). Interestingly, the hyperbranched structure was retained in all the different sized nanoparticles, which is in line with the change of LSPR mentioned above. The hyperbranched structure of randomly arranged short polycrystalline nanorods is fundamentally different from that of the star-like or echinus-like nanostructures (Figure S5), in which the branches radiating from a seeding core lead to weaker intraparticle coupling.[28,42,43]

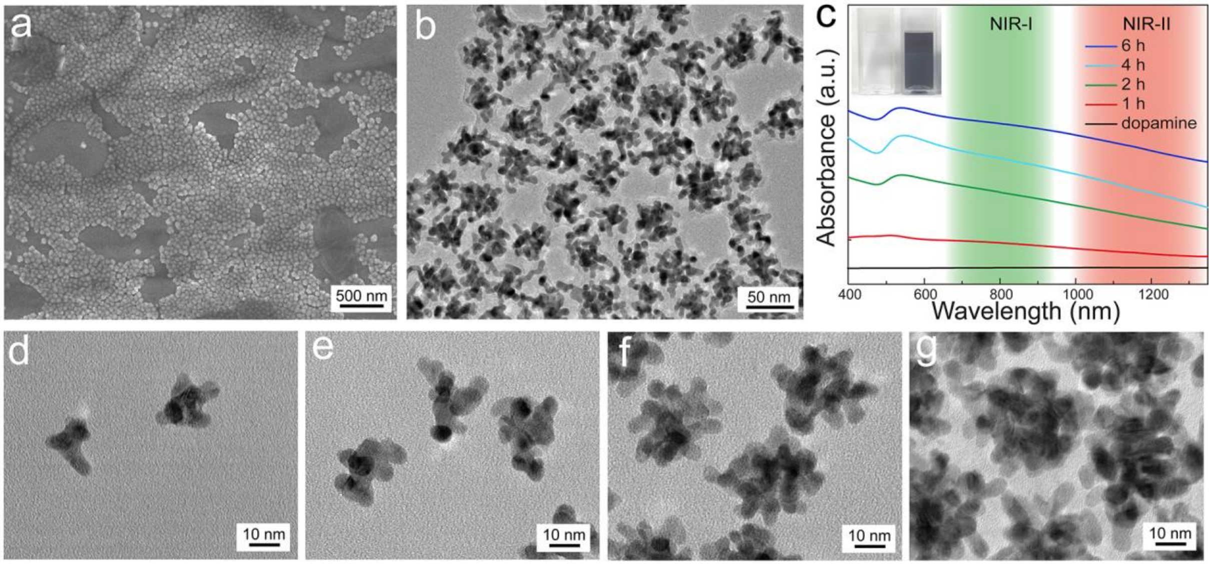

Figure 2. (a) SEM and (b) TEM images of AuPBs of 45 nm in diameter. (c) UV-Vis-NIR absorbance spectra of dopamine and AuPBs at different stages of synthesis. Inset: photographs of dopamine solution (left) and AuPB dispersion (right). TEM images of AuPBs at different time of growth. (d) 1 h, (e) 2 h, (f) 4 h, and (g) 6 h.

Surface chemistry is an essential factor for consideration in the design of nanoparticles for *in vivo* applications. The polydopamine coating also offer the possibility of chemical modification by virtue of the nucleophilic reaction of quinone with thiol and primary amine groups.[41,44,45] As such, the surface of AuPBs was PEGylated using thiolated methoxypoly(ethylene glycol) (PEG-SH) with a molecular weight of 5000 Da (Figure S6). Dynamic light scattering (DLS) measurements (Figure S7) show that introducing PEG grafts increased the hydrodynamic size of the nanocrystals from 44.8 ± 3.0 nm to 56.2 ± 3.7 nm. Polydopamine-coated nanocrystals are negatively charged and showed rapid migration in electrophoresis (Figure S7), which significantly reduced and eventually stopped after PEGylation due to the decrease of surface potential. Note that all the bands in electrophoresis are highly focused, which further confirms the narrow distribution of the AuPBs.

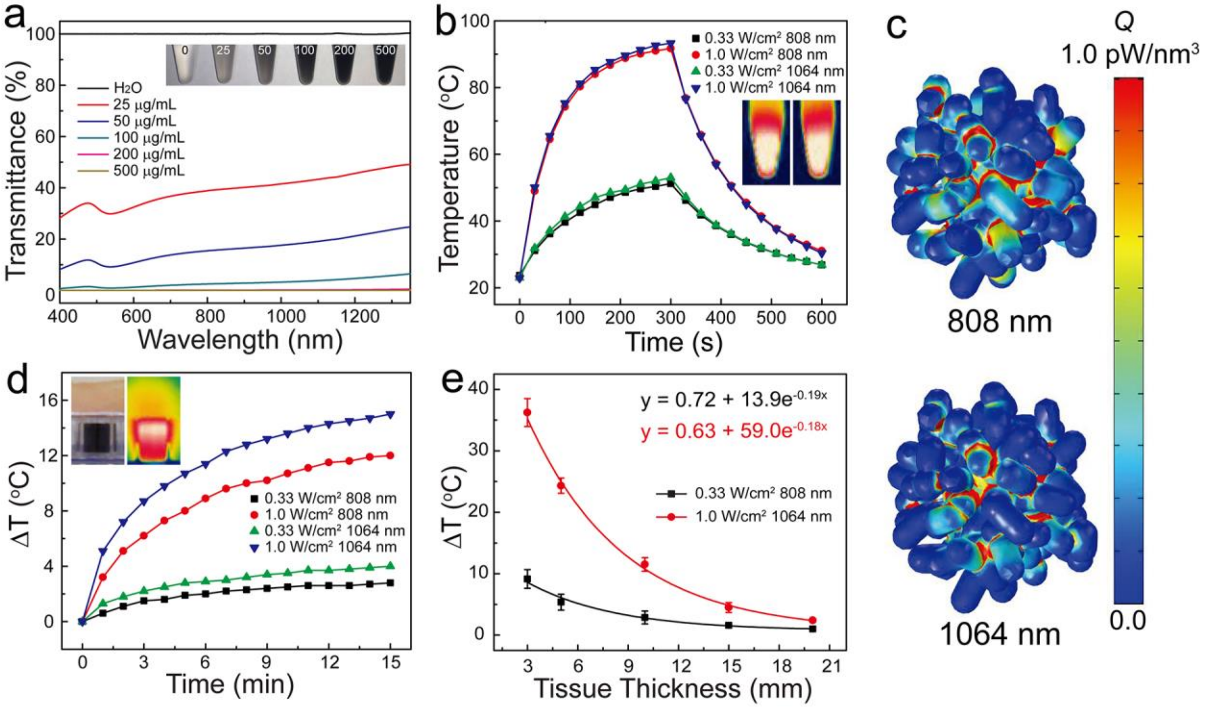

Figure 3. (a) UV-Vis-NIR transmittance of 45 nm AuPBs at different concentrations. Inset: photographs of AuPB dispersions of different concentrations from 0, 25, 50, 100, 200 to 500 μg/mL (from left to right). (b) Temperature curves of AuPBs under NIR-I (808 nm) or NIR-II (1064 nm) laser irradiation at a different power density for 5 min. Inset: infrared thermal images of AuPB irradiated by 808 nm (left) and 1064 nm (right) lasers at 1.0 W/cm^2. (c) Simulation results of the heat power density *Q* inside the AuPBs illuminated by light at 808 nm and 1064 nm. The power density of the incident light was 1.0 W/cm^2 for both wavelengths. (d) Photothermal performance of AuPB dispersion (200 μg/mL) insulated by 1 cm thick chicken breast tissue. Inset: photo (left) and infrared thermal image (right) of AuPB dispersion. (e) Scattered plot of temperature changes of AuPB dispersion (100 μg/mL) under different tissue

depth, with the fitted exponential decay curve. The error bars represent standard deviations (*n* = 3).

Light transmittance through the dispersion is concentration-dependent and nearly all lights in the range of 400-1350 nm are blocked at a low concentration of 0.02% (w:w), suggesting strong light extinction by the plasmonic blackbody (Figure 3a). We next examined photothermal performance of AuPBs in NIR-I and NIR-II using representative laser wavelengths of 808 and 1064 nm for excitation. According to the skin-tolerance threshold set by the America National Standards Institute, a 1064 nm laser has a higher MPE of 1.0 W/cm^2 than that of a 808 nm one (0.33 W/cm^2) (ANSI Z136.1−2007). Therefore, we chose these two critical values to evaluate the photothermal properties. Figure 3b shows that temperature of 45 nm AuPB dispersion (100 μg/mL) in a centrifugation tube rapidly rose up to 93.3 °C for 1064 nm and 91.7 °C for 808 nm within 5 min at a power density of 1.0 W/cm^2. Irradiation at 0.33 W/cm^2 also led to a similar trend of temperature increase at the two wavelengths. Photothermal conversion efficiencies of the AuPB are 88.6% at 808 nm and 80.8% at 1064 nm, respectively (Figure S8). The superior photothermal transduction at the two wavelengths should originate from higher absorption efficiency and smaller scattering cross-section of AuPBs as a result of the small size and strong coupling of hyperbarhched nanostrucure.[20] Simulated spectra are in line with the experimental results, showing that 98.5% of the total extinction comes from absorption (Figure S9). In contrast, 45 nm solid Au nanoparticles only exhibit a narrow LSPR centered at 527 nm with an even greater contribution from scattering (Figure S9). The AuPBs did not show any morphological change after six successive cycles of irradiation (Figure S10). On the other hand, Au nanorods, as commonly used PTT agents, cannot sustain extensive heating.[46,47] We believe that the robust polydopamine coating is a key contributor for the excellent photothermal stability observed.[48,49] Simulation of the electric field reveals that the hyperbranched nanostructure carries optical hot-spots due to strong coupling of the closely-spaced branches (Figure S11). Electric fields at the joints and gaps inside the superstructure were amplified by more than two orders of magnitude, resulting in strong localization of heat generation. The similar heat power density generated by 808 nm and 1064 nm laser explains the comparable photothermal transduction at these two wavelengths (Figure 3c).

To emulate the clinical scenario, we explored the deep tissue photothermal activity using chicken breast as a model tissue. When 10 mm of the tissue was placed between the 45 nm AuPB dispersion (200 μg/mL) and a laser source, efficient heating of the aqueous dispersion was achieved without significant temperature rise inside the tissue (Figure 3d). In presence of the tissue, the 1064 nm laser clearly gave rise to more efficient heating than the 808 nm laser, as a result of more effective tissue penetration. Nevertheless, the difference in final temperature (3.2 °C after 15 min irradiation at 1.0 W/cm^2) is not sufficient to induce significant improvement in PTT efficiency by using NIR-II irradiation. However, taking the safe clinical translation into account, the temperature difference at the MPE of each wavelength is as large as 12.2 °C at a simulated penetration depth of 10 mm, which is expected to cause dramatically improved therapeutic outcome. Moreover, the temperature changes at the MPE of two wavelengths increased exponentially with decreasing tissue thickness, suggesting the substantial energy attenuation by soft tissues even at the NIR-II spectral window (Figure 3e).[50] Our results have confirmed that the benefit of using NIR-II irradiation for PTT primarily lies in the higher MPE, with the better tissue penetration as a minor factor.

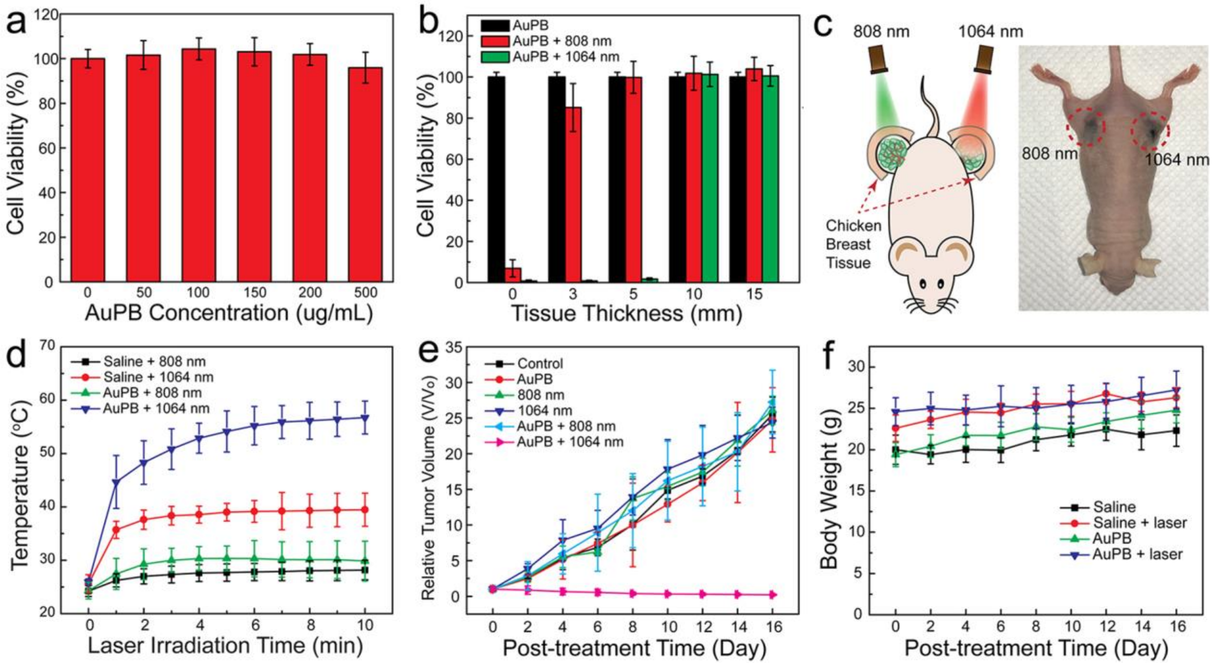

Figure 4. (a) Cell viability of 4T1 cells determined by CCK-8 assay after incubated with different concentrations of AuPBs for 24 h. (b) Cell viability after photothermal treatment (0.33 W/cm^2 for 808 nm and 1.0 W/cm^2 for 1064 nm) with varying thickness of tissue. (c) Schematic illustration of *in vivo* PTT on 4T1-tumor bearing mice covered by 5 mm tissue and photograph of the mouse after laser irradiation. (d) Temperature at tumor region induced by laser treatment (*n*=3). (e) Tumor growth and (f) body weight data of different groups of mice after treatment (*n*=3). The error bars represent standard deviations (*n* = 3).

We further investigated the NIR-I and NIR-II PTT efficacy of the AuPBs *in vitro* and *in vivo*. AuPBs of up to 500 μg/mL did not show any obvious cytotoxicity on 4T1 cells after an incubation of 24 h (Figure 4a). Laser irradiation was applied for 10 min through chicken breast of varying thickness on cells incubated with AuPBs of 100 μg/mL. Under the MPE dose of each laser, NIR-II laser shows efficient photothermal killing of 4T1 cell after passing through tissue of up to 5 mm thick (Figure 4b), whereas NIR-I laser can only induce prominent cell death in absence of any tissue. This is in accordance to the result in Figure 3e, since significant cell killing occurs only when temperature is well above 42 °C.[22]

Photothermal therapeutic capability of the PEGylated AuPBs was assessed on subcutaneous xenograft 4T1 mouse tumor model (Figure 4c). 4T1-tumor bearing mice were injected intratumorally with 100 μL of an AuPB dispersion at 100 μg/mL. To simulate a deeper tumor, the outer area of the tumors were also wrapped with 5-mm chicken breast tissue. Then, tumors were exposed to laser irradiation of MPE dose and the temperature at the tumor site was monitored by a probe thermometer (Figure 4d) placed underneath the tissue. The temperature of the AuPB-injected tumor exposed to 1064 nm laser increased rapidly from 25 °C to more than 50 °C in 3 min and levelled off after 5 min, while the maximum temperature of the saline-injected ones was around 39 °C. In contrast, mice irradiated with a 808 nm laser showed marginal temperature elevation in both groups. Such difference in tumor temperature is consistent with the *in vitro* results (Figure 4b). To quantitatively evaluate the photothermal ablating of tumor by different lasers, the tumor sizes were continuously monitored for 16 days after irradiation (Figure 4e). Only the tumor injected with AuPBs under 1064 nm laser irradiation shows inhibited tumor growth, while no significant therapeutic results can be observed on 808 nm laser-irradiated tumor with AuPBs. Without laser irradiation, the AuPB-injected tumor showed a quick growth similar to the saline-injected ones, indicating that AuPBs themselves are not able to inhibit tumor growth. Similarly, the tumor irradiated by lasers without AuPBs failed to cause any delay in tumor growth since there is no obvious temperature increase on tumor site. Moreover, the body weight of all groups consistently grew during 16 days, indicating the safety of all treatment conditions (Figure 4f). These results definitely substantiate the value of using NIR-II rather than NIR-I for *in vivo* PTT.

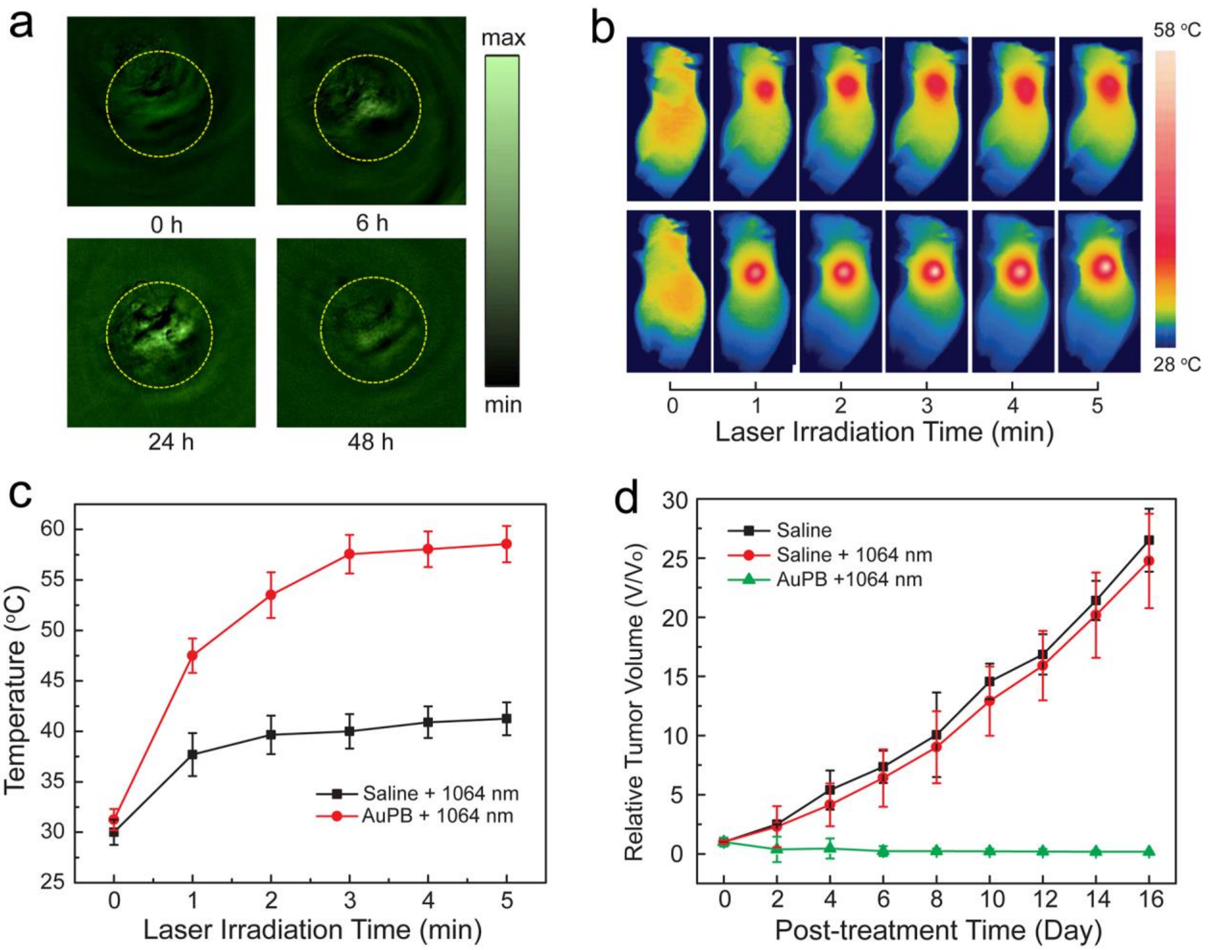

Figure 5. (a) *In vivo* photoacoustic imaging of tumor region (highlighted by yellow circles) acquired at 1064 nm excitation at different time points. (b) Infrared thermal images of 4T1 tumor-bearing mice under 1064 nm laser irradiation (1.0 W/cm^2) after systemic administration of saline and AuPBs at postinjection time for 24 h. (c) Temperature at tumor region induced by 1064 nm laser treatment. The error bars represent standard deviations (*n* = 3). (d) Relative tumor volume of different groups of mice after treatment. The error bars represent standard deviations (*n* = 3).

The uniform and compact size of PEGylated AuPBs is beneficial for passive targeting of solid tumors by the enhanced permeability and retention (EPR) effect.[51] NIR-II mediated PTT was further validated by intravenous injection of AuPBs. After the injection of AuPBs, photoacoustic amplitude at the tumour site increased gradually, and reached its peak value of 4.7 folds of the tumor background signal 24 h post-injection, indicating accumulation of the AuPBs at the tumor region by passive targeting (Figure 5a, S12). Therefore, photothermal ablation using 1064 nm laser was applied 24 h after the injection of AuPBs. The temperature at tumor sites rose up rapidly from 30 °C to more than 55 °C within 3 min, which is considerably higher than that of saline-treated group exposed to the same dosage (Figure 5b,c). After the PTT treatment, tumor sizes were continuously monitored for 16 days. Laser irradiation successfully inhibited the tumor growth of AuPB-injected mice (Figure 5d), while the same laser exposure caused a negligible difference with mice injected with saline. The body weights of all groups maintained a normal trend of growth in the 16 days, suggestive of the tolerability of our AuPBs (Figure S13). The therapeutic outcome is further confirmed by hematoxylin and eosin staining and immunofluorescent staining of caspase-3 in tumors and various organs (Figure S14). PAI of different organs show that accumulation of the AuPBs in reticuloendothelial system (RES) organs such as liver and spleen, which is commonly observed for nanocarriers larger than the size threshold (5-6 nm) of glomerular filtration in the kidneys.[52] However, no obvious histopathological damage was found in liver, spleen, and kidney of AuPB and saline treated groups after PTT because of the localized treatment of PAI-guided PTT and the tolerability of AuPB-PEG. Nuclear dissociation was clearly observed at tumor tissue of AuPB-injected mice after PTT, suggesting necrosis and apoptosis of cancer cells. Furthermore, immunofluorescence staining of caspase-3 clearly show strong green fluorescence in the cancer cells (Figure S14b), revealing apoptosis of the cells in AuPB-injected mice after PTT, whereas no obvious apoptosis was detected in saline control group. These results verify the efficacy and safety of NIR-II PTT mediated by AuPBs *in vivo* at a cellular level, supporting the potential clinical application of NIR-II PTT.

CONCLUSION

In summary, we have developed a hyperbranched plasmonic Au superstructure of controllable sizes, which exhibit nearly perfect blackbody absorption in a size smaller than 50 nm. Taking advantage of mussel-inspired polydopamine, robust AuBPs can be prepared in large scale by a straightforward one-pot synthesis. The strong intraparticle plasmonic coupling among branches in close proximity produces an intense and uniform absorption across the entire UV-Vis-NIR spectral range. This blackbody property enables us to conduct comparative photothermal therapy in NIR-I and NIR-II windows based on the same photothermal agent. Our results clearly reveal that NIR-II-mediated PTT primarily benefit from higher MPE of the NIR-II light rather than the deeper tissue penetration favoured by longer wavelength. We envision that AuPB as a compact broadband nano-absorber holds great potential for a wide range of light-mediated applications, such as energy conversion, photonics and nanomedicine.

METHODS

Synthesis of Au Plasmonic Blackbody (AuPB). Au plasmonic blackbody (AuPB) was prepared by a one-pot method. Typically, 3.6 mL of 4 mg/mL dopamine was added into 72 mL of TRIS buffer under vigorous stirring. After 3 min, 7.2 mL of 0.1 wt% $HAuCl_4$ were injected into the solution. The color of the solution immediately turned to pale yellow, and gradually changed to black. The reaction solution was stirred for 8 h. The 45 nm AuPBs were purified by centrifugation (12000 rcf, 10 min) and was stored in H_2O at 4 °C for further use. The yield of AuPB was measured to be 37.5% by using inductively coupled plasma mass spectroscopy (ICP-MS). The size of the AuPBs can be modulated by varying the concentration ratio between Au precursor and dopamine.

Surface Modification of AuPBs. AuPBs were surface conjugated with HS-PEG (Mw = 5k Da) for improved stability in physiological environment. 2 mL of AuPBs were dispersed in 6 mL of bicine buffer with stirring, followed by adding 20 mg HS-PEG (Mw = 5k Da). The reaction was stirred for 36 h. The AuPB-PEG were obtained by centrifugation. After three times of washing with water, the products were stored in H_2O at 4 °C for further use.

Calculation of the Photothermal Conversion Efficiency. The photothermal conversion efficiency of AuPBs was determined according to a previously reported method. Detailed calculation is given as following:

The total energy input and dissipation from the system can be summarized as below:

$$\sum_i m_i C_{p,i} \frac{dT}{dt} = Q_{NP} + Q_{sys} - Q_{diss} \qquad (1)$$

where m and C_p are mass and heat capacity of system components, including AuPBs, solvent (2.0 mL), and quartz cuvette (5.66 g). T is the solution temperature, Q_{NP} is the energy input from AuPBs, Q_{sys} is the energy input from cuvette containing solvent in the absence of AuPBs, and Q_{diss} is heat dissipation from the system to the surroundings.

The laser-induced heat input term, Q_{NP}, can be also expressed as:

$$Q_{NP} = I(1 - 10^{-A_\lambda})\eta \qquad (2)$$

where I is incident laser power in W, A_λ is the absorbance of AuPBs at wavelength λ, and η is the photothermal transduction efficiency.

The heat dissipation of system term Q_{diss} is linear with system temperature:

$$Q_{diss} = hS(T - T_{surr}) \tag{3}$$

where h is heat transfer coefficient, S is the exposed surface area of the cuvette, and T_{surr} is the temperature of the surroundings.

When the temperature reaches an equilibrium (T_{max}), $\frac{dT}{dt} = 0$. Therefore, Eq. 1 becomes:

$$0 = Q_{NP} + Q_{sys} - Q_{diss} \tag{4}$$

Thus, the energy input is equal to the energy dissipated:

$$Q_{NP} + Q_{sys} = Q_{diss} = hS(T_{max} - T_{surr}) \tag{5}$$

When light is turned off, the heat input terms become zero, Eq. 1 becomes:

$$\sum_i m_i C_{p,i} \frac{dT}{dt} = -Q_{diss} = -hS(T - T_{surr}) \tag{6}$$

Rearranging Eq. 6 would give:

$$dt = -\frac{\sum_i m_i C_{p,i}}{hS} \frac{dT}{T - T_{surr}} \tag{7}$$

Integration of Eq. 7 gives:

$$t = -\frac{\sum_i m_i C_{p,i}}{hS} ln \frac{T - T_{surr}}{T_{max} - T_{surr}} \tag{8}$$

And the system time constant τ_s is defined as:

$$\tau_s = \frac{\sum_i m_i C_{p,i}}{hS} \tag{9}$$

A dimensionless θ is introduced:

$$\theta = \frac{T - T_{surr}}{T_{max} - T_{surr}} \tag{10}$$

Substituting Eq. 9 and 10 into Eq. 8 gives:

$$t = -\tau_s \ln \theta \tag{11}$$

Thus, the time constant for system heat transfer τ_s can be determined by linear regression of the time data *vs.* negative natural logarithm of θ. Therefore, hS can be determined by measuring the rate of temperature drop when the laser is off.

Q_{sys} can be measured directly as:

$$Q_{sys} = hS(T_{max,H_2O} - T_{surr}) \tag{12}$$

The photothermal efficiency can be calculated by equation as below:

$$\eta = \frac{hS(T_{max} - T_{surr}) - Q_{diss}}{I(1 - 10^{-A_\lambda})} \tag{13}$$

Electromagnetic Simulations. Modeling of the AuPBs was performed using the finite element method (COMSOL Mutiphysics 5.0, RF module). The AuPB nanoparticle was constructed by joining short rods in a fashion that matches the TEM images as close as possible. The dimensions of the rods were randomly chosen, with the diameter ranging from 4 nm to 6 nm and the length ranging from 6.5 nm to 11 nm. The overall size of the AuPB was around 45 nm. The dielectric function of Au was adopted from the experiment data by Johnson and Christy with a correction concerning the surface scattering of the small rods. The scattered field was then solved with a linearly polarized background field. Heat power density generated within the AuPB was calculated as the Ohmic loss inside the metal with the background field intensity of 1 W/cm^2.

Cytotoxicity Assay. 4T1 cancer cells were cultured in Dulbecco's modified Eagle's medium (DMEM) mixed with 1.5 g/L sodium biocarbonate, 10% fetal bovine serum (FBS) and 1% streptomycin, with 5 % CO_2 at 37 °C. A standard Cell Counting Kit-8 (CCK-8) was utilized to analyze the cytotoxicity of AuPBs following a general protocol. Briefly, 4T1 cells were seeded in a 96-well plate with the concentration of 50 000 cells/well. After a 24 h incubation at 37 °C in an atmosphere of 5% CO_2 and 95% air incubator, AuPBs of different final concentrations were incubated with cells for 24 h. Then, each well was washed three times with PBS to remove the free AuPBs. 10 μL of CCK-8 solution was added to each well of the 96-well plate to incubate for another 2 h. The amount of an orange formazan dye, produced by the reduction of WST-8 (active gradient in CCK-8) by dehydrogenases in living cells, is directly proportional to the quantity of living cells in the well. Therefore, by measuring the absorbance of each well at 450 nm using a microplate reader, cell viability could be determined by calculating the ratio of absorbance of experimental wells to that of the control cell wells. All experiments were triplicated, and results were averaged.

***In Vitro* PTT in NIR-I and NIR-II Window.** Briefly, 4T1 cells were seeded in a 96-well plate with the concentration of 50000 cells/well and each sample well was spaced out by an empty well. After a 24 h incubation at 37 °C in an atmosphere of 5% CO_2 and 95% air incubator, 100 uL of AuPB (100 μg/mL) was incubated with cells for 24 h. Then, wells were covered by a chicken breast tissue of different thickness (0, 3, 5, 10, 15, and 20 mm), followed by exposed to 808 nm laser or 1064 nm laser for 10 min. After incubation for another 12 h, the wells were washed three times with PBS to remove the free AuPBs. The photothermal cytotoxicity was evaluated by CCK-8 as described above. All experiments were triplicated, and results were averaged.

Mouse Tumor Model. All of our animal experiments were conducted in compliance with the guidelines established by the Institutional Animal Care and Use Committee (IACUC), Sing Health. For tissue thickness-dependent photothermal therapy, the tumors were established on female NCr nude mice by subcutaneous injection of two million 4T1 cells suspended in 0.2 mL DMEM (10% FBS, 1% antibiotics) into both sides of the back of mice. For photothermal therapy in second near-infrared window (NIR-II PTT), two million 4T1 cells suspended in 0.2 mL

DMEM (10% FBS, 1% antibiotics) were subcutaneously injected in the shoulder of a female NCr nude mice. Tumors were grown until a single aspect was ≈ 7 mm (10-15 days) before being used for photothermal treatment.

***In Vivo* PTT in NIR-I and NIR-II Window.** Female NCr nude mice bearing xenograft 4T1 tumors on the left and right sides of the back were intratumorally injected with 100 µL of AuPB solution (100 µg/mL) or saline. A piece of chicken breast tissue (5 mm) was placed on the top of the tumor to mimic the deep tissue environment. Afterwards, tumors covered by chicken breast tissue were exposed to 808 nm laser (0.33 W/cm^2) or 1064 nm laser (1.0 W/cm^2) for 10 min. Temperature of tumor region was monitored by a type K/J thermocouple dual input thermometer embedded under chicken breast tissue. After photothermal treatment, tumor sizes of mice were measured by a caliper every other day for 16 days. Tumor volume was calculated as follows: volume = (tumor length) × (tumor width)^2/2. Relative tumor volume was calculated as V/V_o (V_o was the initial tumor volume).

Photoacoustic Tomography (PAT) System for Tumor Imaging at 1064 nm. A home-made PAT system was used for PAI of tumor. The laser source is 1064 nm Nd:YAG laser (Continuum, Surelite Ex) that can generate 5 ns pulses at 10 Hz repetition rate. The 1064 nm beam was delivered to the PAT system with single-detector circular scanning geometry. The photoacoustic signal generated by the tumor was received by an ultrasound transducer (V323-SU/2.25 MHz, Olympus NDT) with a 13 mm active area and 70% nominal bandwidth. The signals from the tumor area were acquired by continuously rotating the transducer in a circular motion. The collected photoacoustic signals were subsequently amplified, band-pass filtered by an ultrasound pulser/receiver unit (Olympus NDT, 5072PR) and then digitized and recorded by a PC with a DAQ (data acquisition) card (25 Ms/s, GaGe, compuscope 4227). The acquired signals were used to reconstruct the PAI of the tumor using a delay-and-sum back projection algorithm. Animal PAI experiments were performed in accordance with the approved guidelines and regulations, and were approved by the Institutional Animal Care and Use committee of Nanyang Technological University, Singapore (Animal Protocol Number ARF-SBS/NIE-A0263).

***In Vivo* NIR-II PTT.** Female NCr nude mice bearing 4T1 xenograft tumors were administered with AuPB solution (200 µL, 2 mg/mL) or saline (200 µL) *via* tail vein injection ($n = 3$). At 24 h post injection, tumor regions of living mice were exposed to 1064 nm laser at 1.0 W/cm^2. IR thermal camera was used to monitor the temperature of tumor region every 1 min for 5 min during irradiation. After photothermal treatment, sizes of tumors were measured by a caliper every other day for 16 days. Tumor volume was calculated as follows: volume = (tumor length) × (tumor width)^2/2. Relative tumor volume was quantified as V/V_o (V_o was the initial tumor volume). According to the standard animal protocol, mice with tumors larger than 1000 mm^3 should be euthanized.

Histological Analysis. After NIR-II PTT, mice treated with AuPB or saline were sacrificed (n = 3). Livers, spleens, kidneys and tumors were fixed in 4% paraformaldehyde. Then paraffin embedded sectioning was performed and hematoxylin and eosin (H&E) staining was carried out according to standard protocols. Images of slices were captured by a Nikon ECLIPSE 80i microscope. As for immunofluorescence staining, tumors were first fixed in 4% paraformaldehyde for 4 h, dehydrated in 30% sucrose solution for 12 h, and then frozen in Optimal Cutting Temperature (O.C.T.) embedding medium. Sections with a thickness of 10 µm were cut on a cryostat (Leica, CM1950). Sections were subsequently rehydrated in PBS containing 0.1% Triton X-100 for 10 min, followed by incubation with 3% BSA for 1 h at 37 °C. Then sections were stained with cleaved caspase-3 antibody for 1 h. Slides were subsequently washed three times by PBS and then counterstained with Alex-488 conjugated donkey anti-rabbit secondary antibody for 30 min at 37 °C. DAPI was then utilized to stain nuclei. Slides were finally mounted by one drop of Fluoromount Aqueous Mounting Medium and then imaged with LSM710 confocal laser scanning microscope (Carl Zeiss, Germany) with the excitation wavelength of 405 nm for DAPI, 488 nm for Alex-488 conjugated antibody.

ASSOCIATED CONTENT

Supporting Information.

The following files are available free of charge. TEM images, DLS results, electrophoresis, photothermal stability, simulation results, and histological analysis (PDF).

The authors declare no competing financial interest.

AUTHOR INFORMATION

Corresponding Author

*Email: kypu@ntu.edu.sg

*Email: hduan@ntu.edu.sg.

Author Contributions

‡These authors contributed equally.

ACKNOWLEDGMENT

This work is supported by Ministry of Education-Singapore (MOE2015-T2-1-112, MOE2013-T3-1-002, and RG49/16).

REFERENCES

(1) Christopher, P.; Xin, H. L.; Linic, S. Visible-Light-Enhanced Catalytic Oxidation Reactions on Plasmonic Silver Nanostructures. *Nat. Chem.* **2011**, *3*, 467-472.

(2) Neumann, O.; Feronti, C.; Neumann, A. D.; Dong, A. J.; Schell, K.; Lu, B.; Kim, E.; Quinn, M.; Thompson, S.; Grady, N.; Nordlander, P.; Oden, M.; Halas, N. J. Compact Solar Autoclave Based on Steam Generation using Broadband Light-Harvesting Nanoparticles. *Proc. Natl. Acad. Sci. USA* **2013**, *110*, 11677-11681.

(3) Huang, X. Q.; Li, Y. J.; Chen, Y.; Zhou, H. L.; Duan, X. F.; Huang, Y. Plasmonic and Catalytic AuPd Nanowheels for the Efficient Conversion of Light into Chemical Energy. *Angew. Chem., Int. Ed.* **2013**, *52*, 6063-6067.

(4) Bae, K.; Kang, G.; Cho, S. K.; Park, W.; Kim, K.; Padilla, W. J. Flexible Thin-Film Black Gold Membranes with Ultrabroadband Plasmonic Nanofocusing for Efficient Solar Vapour Generation. *Nat. Commun.* **2015**, *6*, 10103.

(5) Cheng, L.; Wang, C.; Feng, L. Z.; Yang, K.; Liu, Z. Functional Nanomaterials for Phototherapies of Cancer. *Chem. Rev.* **2014**, *114*, 10869-10939.

(6) Yang, Z. P.; Ci, L. J.; Bur, J. A.; Lin, S. Y.; Ajayan, P. M. Experimental Observation of an Extremely Dark Material Made by a Low-Density Nanotube Array. *Nano Lett.* **2008**, *8*, 446-451.

(7) Huang, J. F.; Liu, C. X.; Zhu, Y. H.; Masala, S.; Alarousu, E.; Han, Y.; Fratalocchi, A. Harnessing Structural Darkness in the Visible and Infrared Wavelengths for a New Source of Light. *Nat. Nanotechnol.* **2016**, *11,* 60-66.

(8) Zhou, L.; Tan, Y. L.; Ji, D. X.; Zhu, B.; Zhang, P.; Xu, J.; Gan, Q. Q.; Yu, Z. F.; Zhu, J. Self-Assembly of Highly Efficient, Broadband Plasmonic Absorbers for Solar Steam Generation. *Sci. Adv.* **2016**, *2,* 1501227.

(9) Mizuno, K.; Ishii, J.; Kishida, H.; Hayamizu, Y.; Yasuda, S.; Futaba, D. N.; Yumura, M.; Hata, K. A Black Body Absorber from Vertically Aligned Single-Walled Carbon Nanotubes. *Proc. Natl. Acad. Sci. USA* **2009**, *106,* 6044-604710.

(10) Anker, J. N.; Hall, W. P.; Lyandres, O.; Shah, N. C.; Zhao, J.; Van Duyne, R. P. Biosensing with Plasmonic Nanosensors. *Nat. Mater.* **2008**, *7*, 442-453

(11) Wang, H.; Brandl, D. W.; Nordlander, P.; Halas, N. J. Plasmonic Nanostructures: Artificial Molecules. *Acc. Chem. Res.* **2007**, *40,* 53-62.

(12) Ma, Y. Y.; Li, W. Y.; Cho, E. C.; Li, Z. Y.; Yu, T. K.; Zeng, J.; Xie, Z. X.; Xia, Y. N. Au@Ag Core-Shell Nanocubes with Finely Tuned and Well-Controlled Sizes, Shell Thicknesses, and Optical Properties. *ACS Nano* **2010**, *4*, 6725-6734.

(13) Song, J. B.; Huang, P.; Duan, H. W.; Chen, X. Y. Plasmonic Vesicles of Amphiphilic Nanocrystals: Optically Active Multifunctional Platform for Cancer Diagnosis and Therapy. *Acc. Chem. Res.* **2015**, *48*, 2506-2515

(14) Aydin, K.; Ferry, V. E.; Briggs, R. M.; Atwater, H. A. Broadband Polarization-Independent Resonant Light Absorption Using Ultrathin Plasmonic Super Absorbers. *Nat. Commun.* **2011**, *2*, 517.

(15) Cui, Y. X.; Fung, K. H.; Xu, J.; Ma, H. J.; Jin, Y.; He, S. L.; Fang, N. X. Ultrabroadband Light Absorption by a Sawtooth Anisotropic Metamaterial Slab. *Nano Lett.* **2012**, *12,* 1443-1447.

(16) Hogan, N. J.; Urban, A. S.; Ayala-Orozco, C.; Pimpinelli, A.; Nordlander, P.; Halas, N. J. Nanoparticles Heat through Light Localization. *Nano Lett.* **2014**, *14,* 4640-4645.

(17) Nie, Z. H.; Petukhova, A.; Kumacheva, E. Properties and Emerging Applications of Self-Assembled Structures Made from Inorganic Anoparticles. *Nat. Nanotechnol.* **2010**, *5*, 15-25

(18) Song, J. B.; Zhou, J. J.; Duan, H. W. Self-Assembled Plasmonic Vesicles of SERS-Encoded Amphiphilic Gold Nanoparticles for Cancer Cell Targeting and Traceable Intracellular Drug Delivery. *J. Am. Chem. Soc.* **2012**, *134*, 13458-13469.

(19) Liu, D. L.; Zhou, F.; Li, C. C.; Zhang, T.; Zhang, H. H.; Cai, W. P.; Li, Y. Black Gold: Plasmonic Colloidosomes with Broadband Absorption Self-Assembled from Monodispersed Gold Nanospheres by Using a Reverse Emulsion System. *Angew. Chem., Int. Ed.* **2015**, *54*, 9596-9600.

(20) Jain, P. K.; Lee, K. S.; El-Sayed, I. H.; El-Sayed, M. A. Calculated Absorption and Scattering Properties of Gold Nanoparticles of Different Size, Shape, and Composition: Applications in Biological Imaging and Biomedicine. *J. Phys. Chem. B* **2006**, *110*, 7238-7248.

(21) Ayala-Orozco, C.; Urban, C.; Knight, M. W.; Urban, A. S.; Neumann, O.; Bishnoi, S. W.; Mukherjee, S.; Goodman, A. M.; Charron, H.; Mitchell, T.; Shea, M.; Roy, R.; Nanda, S.; Schiff, R.; Halas, N. J.; Joshi, A. Au Nanomatryoshkas as Efficient Near-Infrared Photothermal Transducers for Cancer Treatment: Benchmarking against Nanoshells. *ACS Nano* **2014**, *8*, 6372-6381.

(22) Yun, S. H.; Kwok, S. J. J. Light in Diagnosis, Therapy and Surgery. *Nat. Biomed. Eng.* **2017**, *1*, 0008.

(23) Abadeer, N. S.; Murphy, C. J. Recent Progress in Cancer Thermal Therapy Using Gold Nanoparticles. *J. Phys. Chem. C* **2016**, *120*, 4691-4716.

(24) Song, J. B.; Pu, L.; Zhou, J. J.; Duan, B.; Duan, H. W. Biodegradable Theranostic Plasmonic Vesicles of Amphiphilic Gold Nanorods. *ACS Nano* **2013**, *7*, 9947-9960.

(25) Jiang, Y.; Pu, K. Advanced Photoacoustic Imaging Applications of Near-Infrared Absorbing Organic Nanoparticles. *Small* **2017**, *13*, 1700710.

(26) Jaque, D.; Maestro, L. M.; del Rosal, B.; Haro-Gonzalez, P.; Benayas, A.; Plaza, J. L.; Rodriguez, E. M.; Sole, J. G. Nanoparticles for Photothermal Therapies. *Nanoscale* **2014**, *6*, 9494-9530.

(27) Smith, A. M.; Mancini, M. C.; Nie, S. M. Second Window for *In Vivo* Imaging. *Nat. Nanotechnol.* **2009**, *4*, 710-711.

(28) Vijayaraghavan, P.; Liu, C. H.; Vankayala, R.; Chiang, C. S.; Hwang, K. C. Designing Multi-Branched Gold Nanoechinus for NIR Light Activated Dual Modal Photodynamic and Photothermal Therapy in the Second Biological Window. *Adv. Mater.* **2014**, *26*, 6689-6695.

(29) Jiang, Y.; Upputuri, P. K.; Xie, C.; Lyu, Y.; Zhang, L.; Xiong, Q.; Pramanik, M.; Pu, K. Broadband Absorbing Semiconducting Polymer Nanoparticles for Photoacoustic Imaging in Second Near-Infrared Window. *Nano Lett.* **2017**, *17*, 4964-4969.

(30) Antaris, A. L.; Chen, H.; Cheng, K.; Sun, Y.; Hong, G. S.; Qu, C. R.; Diao, S.; Deng, Z. X.; Hu, X. M.; Zhang, B.; Zhang, X. D.; Yaghi, O. K.; Alamparambil, Z. R.; Hong, X. C.; Cheng, Z.; Dai, H. J. A Small-Molecule Dye for NIR-II Imaging. *Nat. Mater.* **2016**, *15*, 235-242.

(31) Ding, X. G.; Liow, C. H.; Zhang, M. X.; Huang, R. J.; Li, C. Y.; Shen, H.; Liu, M. Y.; Zou, Y.; Gao, N.; Zhang, Z. J.; Li, Y. G.; Wang, Q. B.; Li, S. Z.; Jiang, J. Surface Plasmon Resonance Enhanced Light Absorption and Photothermal Therapy in the Second Near-Infrared Window. *J. Am. Chem. Soc.* **2014**, *136*, 15684-15693.

(32) Tsai, M. F.; Chang, S. H. G.; Cheng, F. Y.; Shanmugam, V.; Cheng, Y. S.; Su, C. H.; Yeh, C. S. Au Nanorod Design as Light-Absorber in the First and Second Biological Near-Infrared Windows for *In Vivo* Photothermal Therapy. *ACS Nano* **2013**, *7*, 5330-5342.

(33) Park, J. E.; Kim, M.; Hwang, J. H.; Nam, J. M. Golden Opportunities: Plasmonic Gold Nanostructures for Biomedical Applications based on the Second Near-Infrared Window. *Small Methods* **2017**, *1*, 1600032.

(34) Li, X. J.; Zhou, J. J.; Liu, C. R.; Xiong, Q. R.; Duan, H. W.; Cheung, P. C. K. Stable and Biocompatible Mushroom Beta-Glucan Modified Gold Nanorods for Cancer Photothermal Therapy. *J. Agric. Food Chem.* **2017**, *65*, 9529-9536.

(35) Hou, S.; Hu, X. N.; Wen, T.; Liu, W. Q.; Wu, X. C. Core-Shell Noble Metal Nanostructures Templated by Gold Nanorods. *Adv. Mater.* **2013**, *25*, 3857-3862.

(36) Talapin, D. V.; Nelson, J. H.; Shevchenko, E. V.; Aloni, S.; Sadtler, B.; Alivisatos, A. P. Seeded Growth of Highly Luminescent CdSe/CdS Nanoheterostructures with Rod and Tetrapod Morphologies. *Nano Lett.* **2007**, *7*, 2951-2959.

(37) Lee, H.; Dellatore, S. M.; Miller, W. M.; Messersmith, P. B. Mussel-Inspired Surface Chemistry for Multifunctional Coatings. *Science* **2007**, *318*, 426-430.

(38) Zhou, J. J.; Duan, B.; Fang, Z.; Song, J. B.; Wang, C. X.; Messersmith, P. B.; Duan, H. W. Interfacial Assembly of Mussel-Inspired Au@Ag@ Polydopamine Core-Shell Nanoparticles for Recyclable Nanocatalysts. *Adv. Mater.* **2014**, *26*, 701-705.

(39) Huo, Z. Y.; Tsung, C. K.; Huang, W. Y.; Zhang, X. F.; Yang, P. D. Sub-Two Nanometer Single Crystal Au Nanowires. *Nano Lett.* **2008**, *8*, 2041-2044.

(40) Zhou, J. J.; Wang, P.; Wang, C. X.; Goh, Y. T.; Fang, Z.; Messersmith, P. B.; Duan, H. W. Versatile Core-Shell Nanoparticle@Metal-Organic Framework Nanohybrids: Exploiting Mussel-Inspired Polydopamine for Tailored Structural Integration. *ACS Nano* **2015**, *9*, 6951-6960.

(41) Zhou, J. J.; Xiong, Q. R.; Ma, J. L.; Ren, J. H.; Messersmith, P. B.; Chen, P.; Duan, H. W. Polydopamine-Enabled Approach toward Tailored Plasmonic Nanogapped Nanoparticles: From Nanogap Engineering to Multifunctionality. *ACS Nano* **2016**, *10*, 11066-11075.

(42) Wang, S. J.; Huang, P.; Nie, L. M.; Xing, R. J.; Liu, D. B.; Wang, Z.; Lin, J.; Chen, S. H.; Niu, G.; Lu, G. M.; Chen, X. Y. Single Continuous Wave Laser Induced Photodynamic/Plasmonic Photothermal Therapy Using Photosensitizer-Functionalized Gold Nanostars. *Adv. Mater.* **2013**, *25*, 3055-3061.

(43) Van de Broek, B.; Devoogdt, N.; D'Hollander, A.; Gijs, H. L.; Jans, K.; Lagae, L.; Muyldermans, S.; Maes, G.; Borghs, G. Specific Cell Targeting with Nanobody Conjugated Branched Gold Nanoparticles for Photothermal Therapy. *ACS Nano* **2011**, *5*, 4319-4328.

(44) Park, J.; Brust, T. F.; Lee, H. J.; Lee, S. C.; Watts, V. J.; Yeo, Y. Polydopamine-Based Simple and Versatile Surface Modification of Polymeric Nano Drug Carriers. *ACS Nano* **2014**, *8*, 3347-3356.

(45) Zhou, J. J.; Wang, C. X.; Wang, P.; Messersmith, P. B.; Duan, H. W. Multifunctional Magnetic Nanochains: Exploiting Self-Polymerization and Versatile Reactivity of Mussel-Inspired Polydopamine. *Chem. Mater.* **2015**, *27*, 3071-3076.

(46) Huang, H. C.; Barua, S.; Kay, D. B.; Rege, K. Simultaneous Enhancement of Photothermal Stability and Gene Delivery Efficacy of Gold Nanorods Using Polyelectrolytes. *ACS Nano* **2009**, *3*, 2941-2952.

(47) Taylor, A. B.; Siddiquee, A. M.; Chon, J. W. M. Below Melting Point Photothermal Reshaping of Single Gold Nanorods Driven by Surface Diffusion. *ACS Nano* **2014**, *8*, 12071-12079.

(48) Liu, Y. L.; Ai, K. L.; Lu, L. H. Polydopamine and Its Derivative Materials: Synthesis and Promising Applications in Energy, Environmental, and Biomedical Fields. *Chem. Rev.* **2014**, *114*, 5057-5115.

(49) Liu, Y. L.; Ai, K. L.; Liu, J. H.; Deng, M.; He, Y. Y.; Lu, L. H. Dopamine-Melanin Colloidal Nanospheres: An Efficient Near-Infrared Photothermal Therapeutic Agent for *In Vivo* Cancer Therapy. *Adv. Mater.* **2013**, *25*, 1353-1359.

(50) Bashkatov, A. N.; Genina, E. A.; Kochubey, V. I.; Tuchin, V. V. Optical Properties of Human Skin, Subcutaneous and Mucous Tissues in the Wavelength Range from 400 to 2000 nm. *J. Phys. D: Appl. Phys.* **2005**, *38*, 2543-2555.

(51) Bjornmalm, M.; Thurecht, K. J.; Michael, M.; Scott, A. M.; Caruso, F. Bridging Bio-Nano Science and Cancer Nanomedicine. *ACS Nano* **2017**, *11*, 9594-9613.

(52) Yu, M. X.; Zheng, J. Clearance Pathways and Tumor Targeting of Imaging Nanoparticles. *ACS Nano* **2015**, *9*, 6655-6674.

TOC Graphic

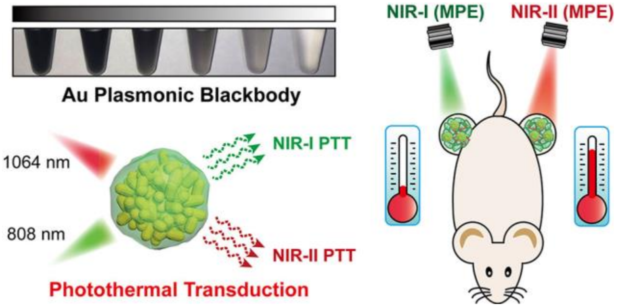
Au Plasmonic Blackbody
1064 nm
808 nm
NIR-I PTT
NIR-II PTT
Photothermal Transduction
NIR-I (MPE)
NIR-II (MPE)